



# Brittle–viscous deformation of vein quartz under fluid-rich lower greenschist facies conditions

H. J. Kjøll<sup>1</sup>, G. Viola<sup>1,2</sup>, L. Menegon<sup>3</sup>, and B. E. Sørensen<sup>1</sup>

<sup>1</sup>Dept. of Geology and Mineral Resources Engineering, Norwegian University of Science and Technology, Trondheim, Norway

<sup>2</sup>Geological Survey of Norway, Trondheim, Norway

<sup>3</sup>School of Geography, Earth and Environmental Sciences, Plymouth University, Plymouth, UK

Correspondence to: H. J. Kjøll (hans.j.k@gmail.com)

Received: 16 December 2014 – Published in Solid Earth Discuss.: 23 January 2015

Revised: 2 May 2015 – Accepted: 16 May 2015 – Published: 11 June 2015

**Abstract.** We studied by Electron BackScatter Diffraction (EBSD) and optical microscopy a coarse-grained (ca. 0.5–6 mm) quartz vein embedded in a phyllonitic matrix to gain insights into the recrystallization mechanisms and the processes of strain localization in quartz deformed under lower greenschist facies conditions, broadly coincident with the brittle–viscous transition. The vein deformed during faulting along a phyllonitic thrust of Caledonian age within the Porsa Imbricate Stack in the Paleoproterozoic Repparfjord Tectonic Window in northern Norway. The phyllonite hosting the vein formed at the expense of a metabasaltic protolith through feldspar breakdown to form interconnected layers of fine, synkinematic phyllosilicates. In the mechanically weak framework of the phyllonite, the quartz vein acted as a relatively rigid body. Viscous deformation in the vein was initially accommodated by quartz basal  $\langle a \rangle$  slip. Under the prevailing deformation conditions, however, dislocation glide- and possibly creep-accommodated deformation of quartz was inefficient, and this resulted in localized strain hardening. In response to the (1) hardening, (2) progressive and cyclic increase of the fluid pressure, and (3) increasing competence contrast between the vein and the weakly foliated host phyllonite, vein quartz crystals began to deform by brittle processes along specific, suitably oriented lattice planes, creating microgouges along microfractures. Nucleated new grains rapidly sealed these fractures as fluids penetrated the actively deforming system. The grains grew initially by solution precipitation and later by grain boundary migration. We suggest that the different initial orientation of the vein crystals led to strain accommodation by different

mechanisms in the individual crystals, generating remarkably different microstructures. Crystals suitably oriented for basal slip, for example, accommodated strain mainly viscously and experienced only minor fracturing. Instead, crystals misoriented for basal slip hardened and deformed predominantly by domainal fracturing. This study indicates the importance of considering shear zones as dynamic systems wherein the activated deformation mechanisms may vary through time in response to the complex temporal and spatial evolution of the shear zone, often in a cyclic fashion.

## 1 Introduction

Deformation of quartz at low-grade metamorphic conditions has been the subject of a vast number of microstructural studies aiming to unravel the mechanisms that control strain accommodation therein and to derive parameters of general validity for the rheology of quartz-rich systems at shallow to mid crustal levels (e.g., Trepmann and Stöckhert, 2009; Stipp et al., 2002; Menegon et al., 2008; Holyoke and Tullis, 2006; Dell'Angelo and Tullis, 1996; Hirth and Tullis, 1992; Stipp and Kunze, 2008; Hirth and Beeler, 2015). In spite of significant recent advances, however, much remains unexplored and unaccounted for, such as (1) the role of fluid–rock interaction on the microstructural development of quartz, (2) the effect of contrasting rheology and of the resulting strain partitioning between matrix and quartz porphyroclasts, and (3) the feedback mechanisms between brittle and viscous processes. Recent technological developments have

made powerful methodologies such as electron backscattered diffraction (EBSD; e.g., Adams et al., 1993; Prior et al., 1999, 2009) readily available. This permits extremely detailed investigations and quantification of microstructures and, thereby, the derivation of refined conceptual models of the deformation mechanisms in quartz at the broadly defined brittle–viscous transition.

Intragrain quartz microstructures characterized by bands of fine new grains in large porphyroclasts have been noted and described as standard for low-grade deformed quartz in a number of studies, both experimental and natural (e.g., Vernooij et al., 2006b; van Daalen et al., 1999; Menegon et al., 2008). These microstructures tend to develop during the very early stages of viscous deformation in quartz and are thus studied to better understand strain localization under very low-grade metamorphic conditions. Four mechanisms have been proposed to explain their occurrence: (1) progressive subgrain rotation recrystallization with subsequent grain boundary sliding (Bestmann and Prior, 2003), (2) intrapore growth by dissolution precipitation (e.g., den Brok and Spiers, 1991; Hippertt and Egydio-Silva, 1996), (3) fracturing along specific crystallographic planes with subsequent fragment rotation (e.g., den Brok, 1992; van Daalen et al., 1999; Vernooij et al., 2006b), and (4) localized recrystallization along Dauphin   twins (Stipp and Kunze, 2008; Menegon et al., 2011). Van Daalen et al. (1999) observed that bands of new grains tend to develop preferentially along the rhomb direction within the deforming crystal. Trepmann et al. (2007) studied further the importance of these microstructures by means of carefully designed experiments, wherein they investigated deformation at the tip of a seismic fault. They could reproduce similar microstructures by deforming moderately wet quartz under high stresses before annealing it quasi-statically under dry conditions.

We aim herein to investigate further how these characteristic microstructures develop in quartz at the brittle–viscous transition in a tectonically active environment wherein fluids and competence contrasts between the actively deforming mineral phases induce cyclic oscillations between brittle and viscous conditions. To do so, we studied in detail the microstructure of a quartz vein embedded in a phyllonitic matrix. The vein, which crystallized statically prior to deformation, permitted an assessment of the influence exerted by the different initial orientations of the deformed quartz crystals on the accommodation of subsequent strain increments by either brittle or viscous processes. The different initial orientations of vein quartz grains caused the development of drastically different end microstructures within a very small volume of rock, thus allowing the critical and comparative analysis of the different deformation mechanisms that acted simultaneously during deformation.

## 2 Geological setting

### 2.1 Regional geological setting and structural framework

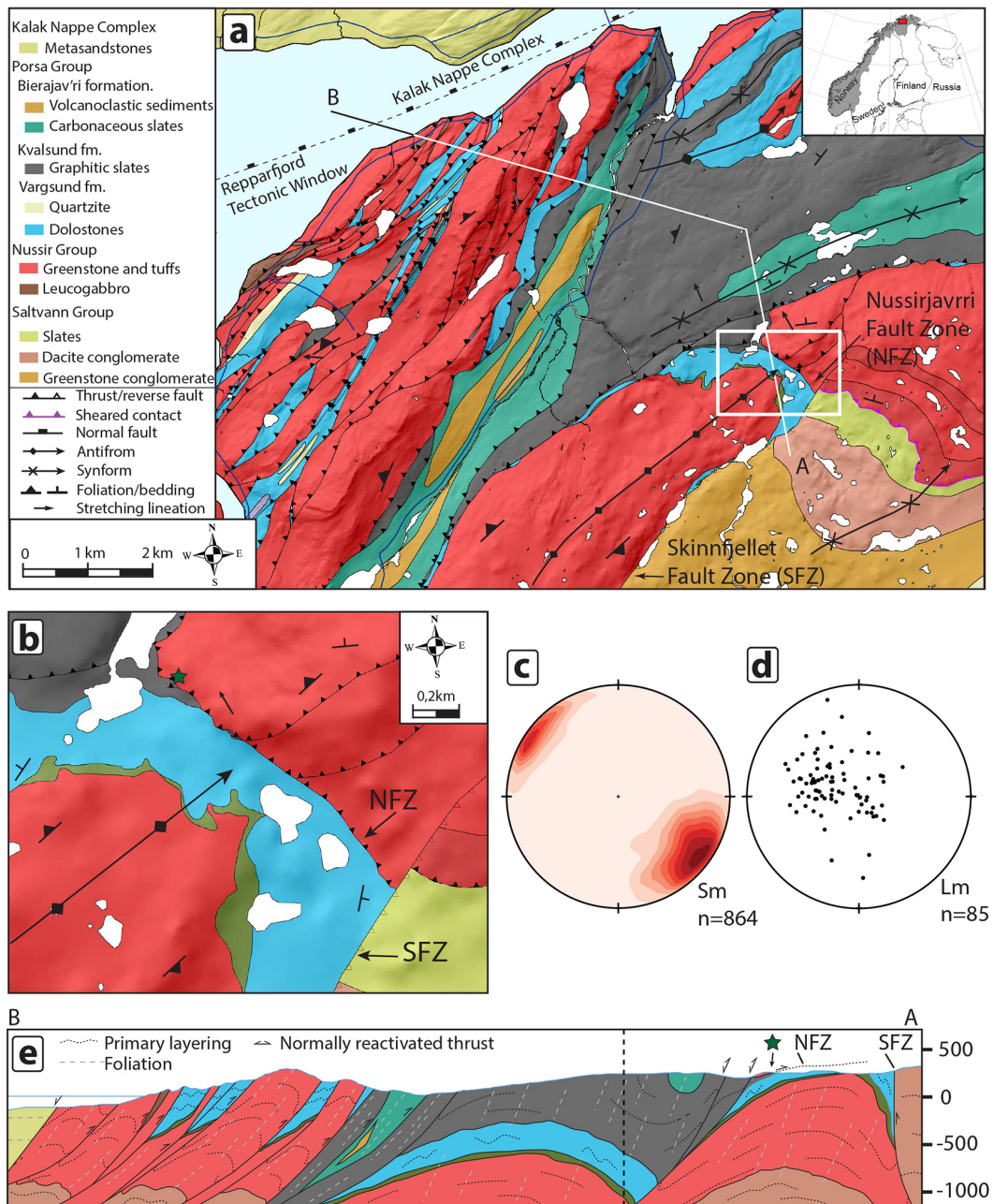
The study area is located within the Repparfjord Tectonic Window (RTW), the northernmost exposed termination of the Fennoscandian Shield in northern Norway (Fig. 1). The RTW is a window through the Scandinavian Caledonides, which in the study area consists of greenschist to amphibolite-facies metapelites, metapsammites and marbles, with intercalated gneissic slivers (e.g., Gee et al., 2008; Roberts, 2003; Torgersen et al., 2014). The RTW exposes a metasupracrustal sequence formed by greenschist to lower amphibolite facies metasedimentary and metavolcanic rocks, ranging from clastic and volcanoclastic rocks to ultramafic and rhyolitic calc-alkaline to tholeiitic volcanic rocks (Pharaoh, 1985; Pharaoh et al., 1983). K–Ar dating suggests that they deformed under greenschist-facies conditions until ca. 1840 million years ago, with formation of kilometer-scale upright folds (e.g., Pharaoh et al., 1982).

The northwesternmost part of the RTW shows a set of strongly deformed tectonic imbricates, stacked up to form the Porsa Imbricate Stack (PIS; Torgersen and Viola, 2014; Fig. 1a). Shortening and imbrication within the PIS occurred during the Silurian Caledonian orogeny, which accommodated overall NW–SE shortening and ca. eastward nappe transport (Rice, 1998). As deformation localized during development of the PIS, discrete thrust faults nucleated on the limbs of inherited Paleoproterozoic folds. These tightened and acquired a SE-vergence during the late stages of shortening of the PIS. The Caledonian overprint within the RTW becomes progressively less penetrative to the SE where the imbricate stack terminates against the sub-vertical Skinnfjellet Fault Zone, a dip-slip reverse fault (SFZ; Fig. 1a). Rocks in the immediate footwall of the floor Caledonian d  collement underwent greenschist facies metamorphism and were openly refolded around NE- moderately to gently plunging fold axes. Regional metamorphism was constrained to 430–410 million years by Dallmeyer et al. (1988) by Ar–Ar dating on rejuvenated micas.

In the north, the SFZ cuts a gently dipping thrust that accommodated southeastward transport at the front of the PIS, the Nussirj  vri Fault Zone (NFZ; Fig. 1a), which is where the studied quartz vein was sampled.

### 2.2 Nussirj  vri Fault Zone

The NFZ is interpreted as an out-of-sequence thrust fault that juxtaposes sub-aqueous extrusive basalts interlayered with clastic to conglomeratic agglomerates and mafic tuffs in the hanging wall against younger slates and dolostones in the footwall. The fault plane is well exposed along strike for ca. 1 km (Fig. 1b). It varies in thickness between 10 cm and several meters, it dips moderately towards the NNW and

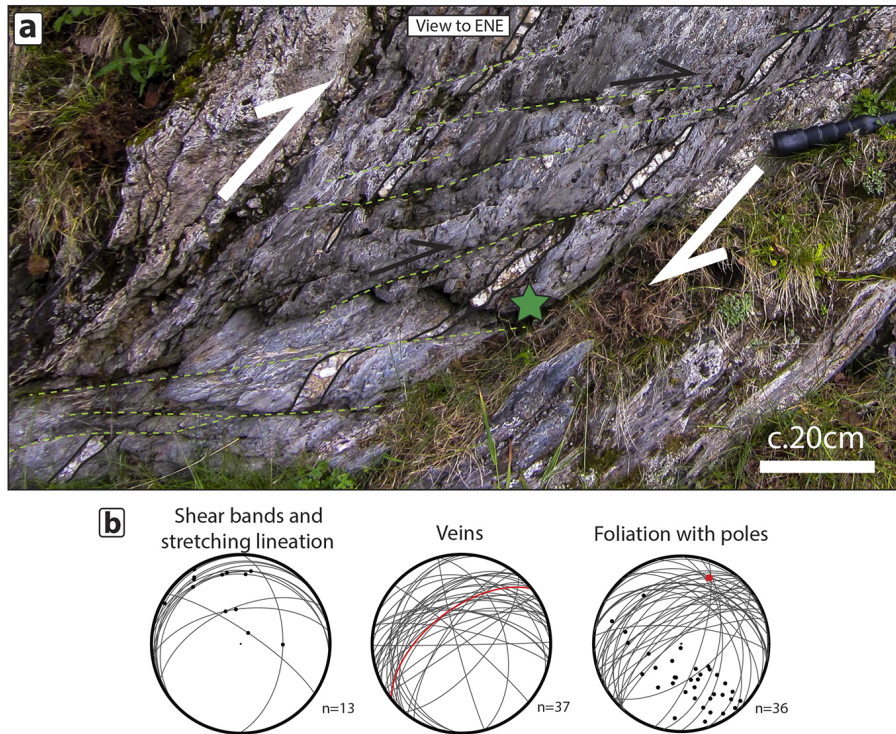


**Figure 1.** (a) 1 : 50 000 geological map of the northwestern part of the Repparfjord Tectonic Window. Doglegged line: trace of cross section in (e). White rectangle: location of detailed map in (b). Inset shows the location of the study area in northern Norway. (b) Close-up of the Nussirjávri Fault Zone (NFZ) and sample location shown by green star. (c and d) Contoured foliation and stretching lineation measurements, respectively, from the mapped area (lower hemisphere projection). (e) Cross section along the doglegged line in (a). Black dashed line: folded primary layering, gray dashed line: axial planar foliation. Green star: sample location.

bears NW plunging stretching lineations. Kinematic indicators, both at the meso- and micro-scale (Fig. 2a), indicate top-to-the-SE reverse kinematics, thus are consistent with the regional transport direction of the PIS as a whole. The NFZ is folded openly around a fold axis plunging gently to moderately towards the NNE, consistent with the geometry of a

sub-regional folding phase of inferred Caledonian age (e.g., Rice, 1998; Pharaoh et al., 1983; Torgersen and Viola, 2014; Fig. 2b).

The NFZ fault core varies in composition as a function of the lithologies affected by deformation. Where the fault deforms graphitic slates, the NFZ has a well-developed my-



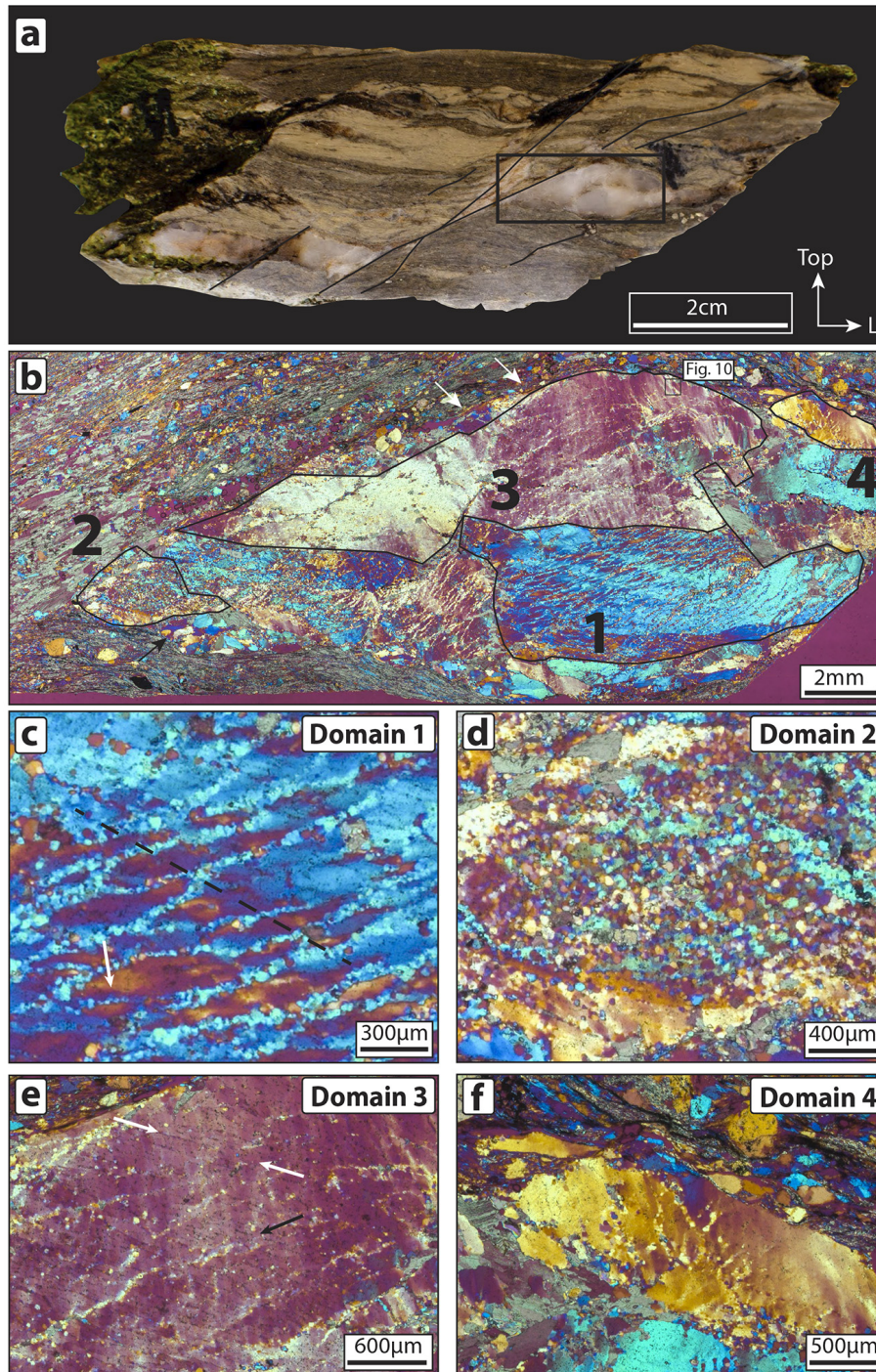
**Figure 2.** (a) Veins (outlined by black lines) cut by gently NNW-dipping shear bands (green dashed lines) that create a pervasive ECC fabric at the outcrop scale. The NFZ fault core is located 2 m farther up. Sample location is indicated by the green star. Hammer handle for scale. (b) Orientation of key structural elements of the NFZ in lower hemisphere projections. Left stereonet: shear bands related to the NFZ and related stretching lineations. Middle stereonet: veins along the NFZ. The sampled vein is indicated by the red great circle. Right stereonet: great circles and poles of NFZ mylonitic and phyllonitic foliation planes indicating that the NFZ is folded around a calculated axis oriented 024/19 as indicated with a red point.

lonitic core. Several large clasts of both graphitic slate and partially decarbonized dolostone are found within the mylonitic foliation. Elsewhere, where the hanging wall porphyritic basalt forms the fault core, a pervasive phyllonitic fabric consisting of chlorite, white mica and fine-grained quartz ( $< 50 \mu\text{m}$ ) together with scattered boudinaged clasts of Na-rich plagioclase usually  $< 500 \mu\text{m}$  in size defines the NFZ (Fig. 4a).

Numerous quartz-carbonate veins and veinlets are transposed along the phyllonitic foliation. They are locally imbricated, confirming the top-to-the-SE kinematics. Locally the mylonitic fabric is deformed by a pervasive extensional crenulation cleavage (ECC; Platt and Vissers, 1980) with individual shear bands dipping gently towards the NNW invariably indicating top-to-the-SE transport, which, in the present geometry, corresponds to southeastward thrusting along the NFZ (Fig. 2a and b). Field relations indicate that vein emplacement was pre- to syntectonic as most veins are either boudinaged or cut by the ECC shear bands. One of these veins forms the subject of our study (green star in Fig. 2a).

### 3 Analytical method

Standard oriented thin sections cut orthogonal to the foliation and parallel to the stretching lineation were used for classic petrographic investigations and to investigate the crystallographic preferred orientation (CPO) of the vein quartz by EBSD analysis at the Scanning Electron Microscope (SEM). To remove surface damage and thereby enhance the diffraction signal, the thin sections were polished using colloidal silica for 5 min (Moen et al., 2003) and placed in a Hitachi VP-SEM with a Nordif UF-1000 EBSD detector (Chen et al., 2012) at a  $70^\circ$  tilt to the horizontal (Prior et al., 1999). To acquire satisfactory pattern quality the accelerating voltage used was 20.0 kV at 35 nA absorbed current. The working distance was set to 25.3 mm and the step size to  $2 \mu\text{m}$ . The data were processed using the open source Matlab toolbox MTEX 3.5.0 (e.g., Bachmann et al., 2010; Mainprice et al., 2011). The confidence index for the produced maps was set at 0.0145. Partitions based on aspect ratio and grain size were used to generate data subsets of the new- and old-grain fractions. Aspect ratio and grain size for the old-grain fraction ranged from 1.3 to 4.0 and 56 to  $200 \mu\text{m}$  respectively, while for the new grains they ranged from 1.6 to 3.0 and 40



**Figure 3.** (a) Studied hand specimen. A discrete shear band cuts through the entire sample and offsets the studied quartz vein. Several second-order shear bands are also visible and some deform the vein with a smaller displacement. Black square: area of (b). Photomicrographs (b–f) are all taken with crossed polarizers and lambda plate inserted. (b) Stacked overview photomicrograph of the studied vein fragment. Black outline distinct textural domains, labeled 1–4. Black square in Domain 3 indicates location of Fig. 10. White arrows: sites of possible dissolution at vein-matrix contact. (c) Close-up of a representative area of Domain 1. Black dashed line: direction of wide extinction bands (WEBs; Derez et al., 2014) seen as red-orange areas. White arrow: bridging band of new grains. (d) Close-up of representative microstructure of Domain 2. (e) Domain 3. White arrows: trace of fluid inclusion plane. Black arrow: direction of band with new grains. (f) Close-up of Domain 4 showing bands of new grains at a relatively high angle to each other.

to 56  $\mu\text{m}$ . Further analysis of the EBSD data was conducted using ImageJ image (Schneider et al., 2012).

## 4 Results

### 4.1 Sample description

The studied sample is from a quartz vein and its host rock at an outcrop (green star in Figs. 1 and 2), where the main NFZ foliation developed at the expense of metabasalt. The vein is cut and offset by top-to-the-SE  $C'$  shear bands that impart the outcrop a pervasive ECC. The hand specimen is a well-foliated phyllonitic rock containing a centimetric clast of the quartz vein bound by and offset along a centimetric scale shear band, with numerous smaller shear bands also deforming the vein (Fig. 3a). The phyllonitic foliation is passively dragged into the shear bands confirming the kinematics determined by field observations (Figs. 2a, 3a and 4a).

The phyllonitic foliation is defined by layers consisting of varying amounts of feldspathic clasts with albitic composition within a phyllosilicate-rich matrix of chlorite and sericitic white mica. The grain size of the phyllonite is very fine, usually < 50  $\mu\text{m}$ , except for some residual dolomitic porphyroclasts, which are up to > 1 mm in size. Feldspar clasts range in size from < 200 to > 1000  $\mu\text{m}$  and are locally asymmetrically boudinaged and deformed by small shear bands. The neck zones of the boudins are commonly filled with new grains of feldspars (Fig. 4a). Small-scale shear bands locally indicate both dextral and sinistral sense of shear, suggesting a component of flattening.

Several euhedral sulfide porphyroblasts, partially broken down to oxides, are dispersed in the phyllonite and within the vein; some are also symmetrically boudinaged and fibrous quartz is present in the neck domains and pressure shadows (Fig. 4b). Sigmoidal dolomite porphyroclasts are commonly observed. Syntaxially filled calcite veinlets occur sub-parallel to the mylonitic foliation. These veinlets generally accommodated more than one opening event (Fig. 4e)

The studied vein clast consists primarily of quartz with only minor primary calcite. Secondary calcite and accessory sulfides are found both within the quartz crystals and along the grain boundaries. Quartz crystals within the vein range in size from < 0.5 to > 6 mm (Fig. 3b) and show neither a clear crystal preferred orientation (CPO; Figs. 6–9b) nor a shape-preferred orientation (SPO). However, the number of primary quartz grains included in the studied thin section is low, so that we cannot rule out that the quartz vein displayed an initial SPO and CPO. In general, the boundaries between the individual grains are slightly irregular but straight, which gives the individual quartz crystals a blocky appearance (Fig. 3b), although the vein-matrix contact is generally more rounded.

### 4.2 Microstructural and EBSD analysis

Because of the marked microstructural differences that we have observed within the quartz vein, we have identified and studied in detail several domains, each characterized by internally consistent microstructures. Our study reports four representative domains that are described individually below. Table 1 and Figs. 6–9 sum up the main CPO elements constrained by petrographic and EBSD analysis.

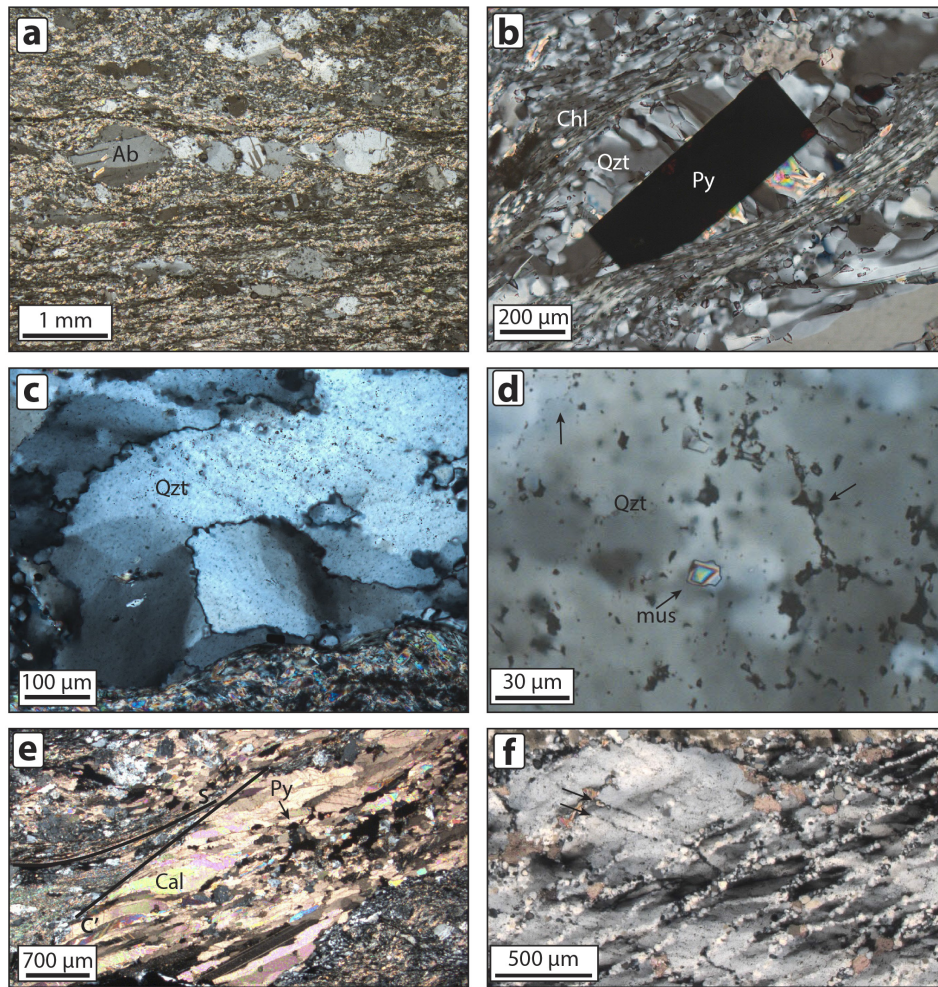
Several quartz crystals contain narrow bands of much finer grains. In the text these grains are referred to as nucleated “new grains” and are distinguished from the parent grains or “old grains” based on aspect ratio, grain size and misorientation angle to neighbor grains. In detail, all grain boundaries were defined as misorientations larger than 10° (e.g., Trepmann et al., 2007).

#### 4.2.1 Domain 1

Domain 1 (Fig. 3b and c) is found within a single crystal measuring 6 × 3 mm. It contains a tightly spaced set of sub-parallel and semi-straight bands of nucleated grains. The bands are sub-parallel to the  $C'$  shear planes that offset the quartz vein. They are continuous for several millimeters and are on average 30  $\mu\text{m}$  thick (1–3 grains thick). We name this microstructure “striped tiger”. Bridges between the most pronounced bands are observed (white arrow in Fig. 3c). The nucleated grains vary in size between ca. 10 and 60  $\mu\text{m}$ , have a slightly elongated shape and constitute ca. 40 % of the area of the domain. Fluid inclusions occur within the bands where they commonly encircle the nucleated grains. Much smaller fluid inclusions (< ca. 2  $\mu\text{m}$ ) are instead abundant and apparently randomly distributed within the host old crystal (Fig. 4d). Some bands also contain small (ca. 50  $\mu\text{m}$ ) calcite grains interspersed among the new quartz grains (Fig. 4f).

The host grain displays undulose extinction, which is defined by wide extinction bands (WEBs; Derez et al., 2014; black dashed line in Fig. 3c). These are sub-parallel to local fluid inclusion traces that also appear to be cut by the bands of new grains (Fig. 4f). WEBs have an antithetic geometry to the large shear band that cuts through and offsets the quartz vein in the hand specimen (Fig. 3a, b and c) and are themselves cut by the bands of new grains (Fig. 3b, c and f).

EBSD analysis of the sub-parallel bands of new grains shows that they range in size between ca. 5 and 50  $\mu\text{m}$  (Fig. 6f and Table 1), and have a different crystallographic orientation from the host (Fig. 6b–d). The  $c$  axis of the host grain in Domain 1 is in the foliation plane at ca. 15° from the stretching lineation and is visualized by the orange color in Fig. 6a and b. The host grain contains a large amount of subgrains that are locally larger than the nucleated grains within the bands. The red color within the old grain (Fig. 6a) represents Dauphiné twins, which accommodate a 60° rotation around the  $c$  axis and are thus not visible under the optical microscope (Frondel et al., 1962). As noted above, there are



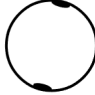



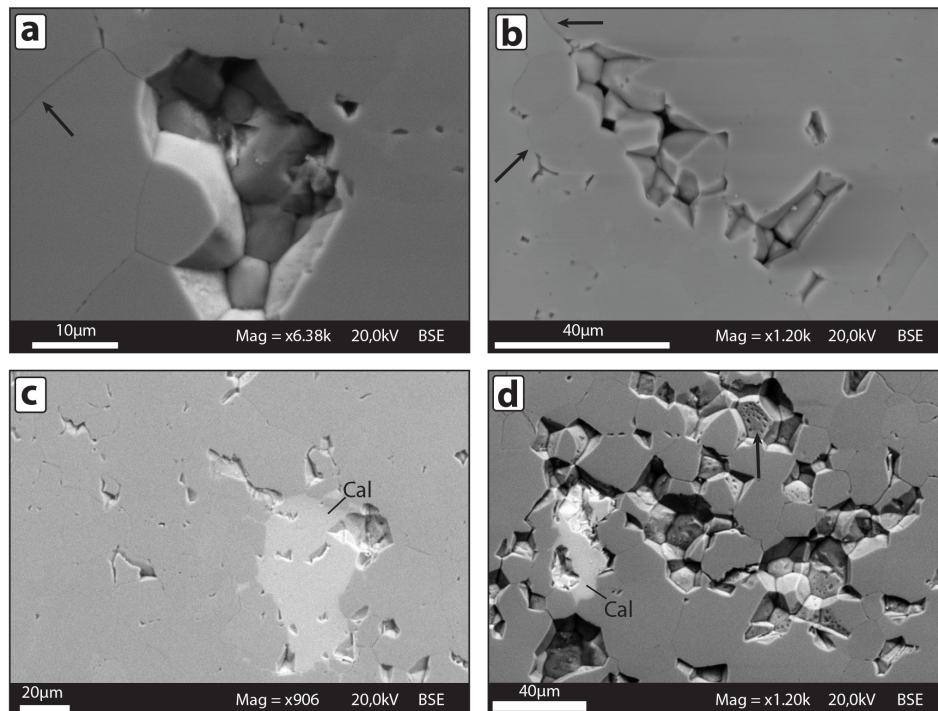
**Figure 4.** All the photomicrographs are taken with crossed polarizers. **(a)** Albitic feldspar crystals asymmetrically cut and offset by dextral shear bands within the sheared, phyllosilicate-rich foliation of the NFZ. Minor recrystallization of the plagioclase can be seen in some of the shear bands. **(b)** Euhedral pyrite crystal partially altered to oxides with fibrous quartz and mica growing in the fringes, surrounded by chlorite. **(c)** Bulging grain boundaries and subgrains indicate low-grade deformation of the vein quartz. **(d)** Small mica grain within a band of new grains in Domain 3. Fluid inclusions outline the new grains (black arrows) and partially define the band. New grains are seen as different shades of gray. **(e)** Calcite veinlet displaying several opening events, with fine-grained quartz at the matrix boundary with large, elongated calcite crystals and smaller equidimensional grains with some interspersed sulfides in the center. Foliation *S* dragged into the *C'* shear band. **(f)** Microcracks sub-parallel to the rhomb plane and WEBS in Domain 1, cut by bands of new grains. Microcracks contain secondary phases (calcite) and show incipient recrystallization of quartz. Bands of new grains also show secondary phases (calcite, muscovite).

two sets of bands in the domain, one pervasively developed and one subordinate. The more developed set contains bands that are sub-parallel to the prism plane of the host old grain (dashed line in the pole figure of the prism, *m*; Fig. 6b) and thus are oriented sub-parallel to the sample-scale *C'* shear band and with an average 25° angle to the foliation, when measured counterclockwise. The less developed bands are seen in the lower left corner of the EBSD map (white arrow in Fig. 6a) and are sub-parallel to the rhomb (dashed line in the pole figure of the rhomb, *{r}*; Fig. 6b) forming an angle of ca. 142° to the foliation, *S*, measured counterclockwise. The new grains within the bands are slightly el-

liptical with an average aspect ratio of 1.63 and average grain size of 15.51 μm (Fig. 6e and f). The new grains have a more scattered *c* axis distribution with a counterclockwise rotation around the *y* axis (Fig. 6c). They display large misorientations (locally >40°) to each other and to the host. The new grains show no to very little internal deformation, and there is no progressive rotation of the lattice when approaching the bands from the host; i.e., the change in misorientation is abrupt (Fig. 6d1 and d2).

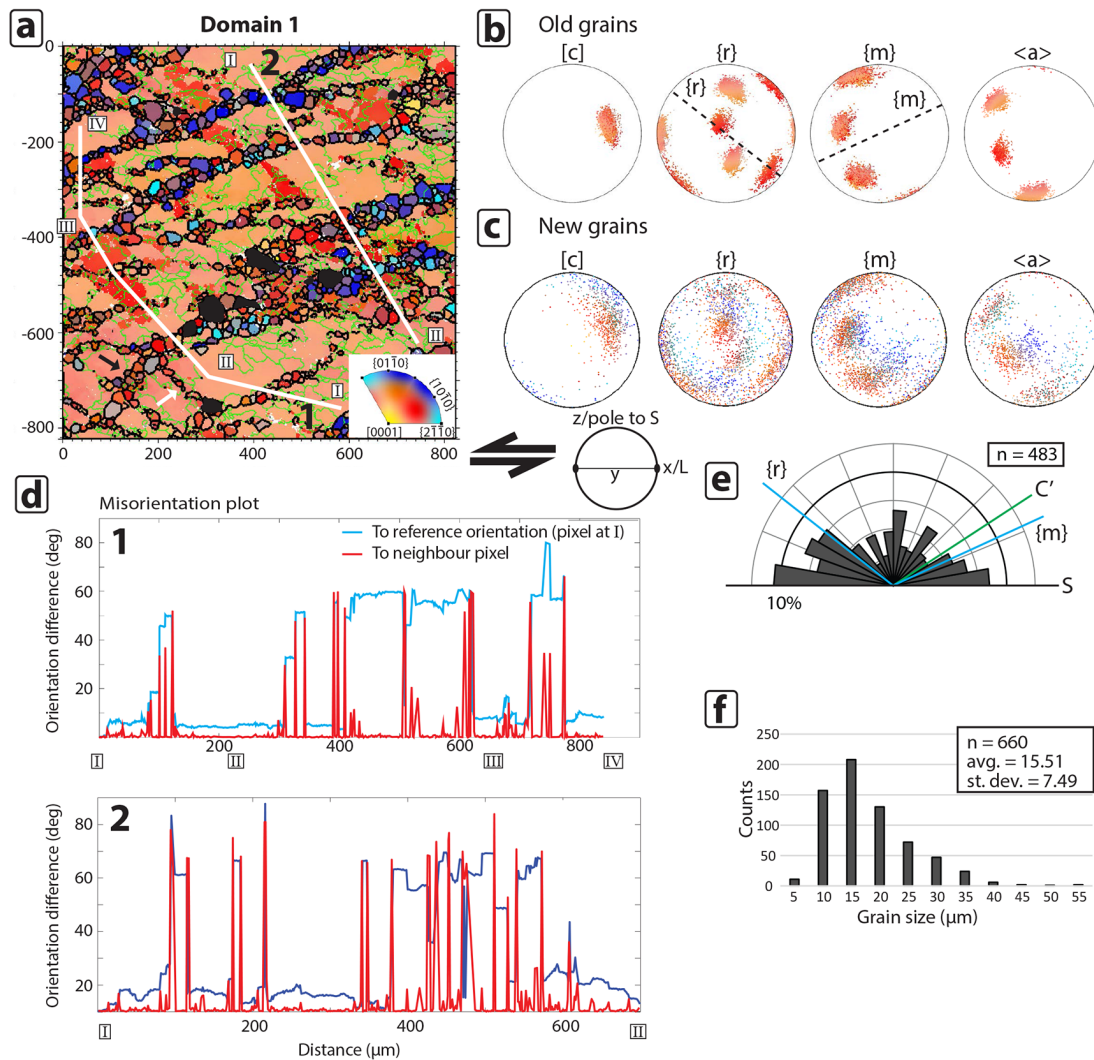
**Table 1.** Summary of microstructures.

Domain	Old-grain <i>c</i> axis orientation	Microstructure type	Orientation of bands of new nucleated grains	Orientation of bands of new nucleated grains	Average grain size ( $\mu\text{m}$ )	Average aspect ratio
1		Pervasive nucleation; “striped tiger” pattern	$\parallel$ to $\{m\}$ and $\parallel$ to $\{r\}$	ca. $25^\circ$ and ca. $142^\circ$	Avg.: 15.51; Max.: 52.46; Min.: 4.47	1.63
2		Dominated by new nucleated grains	$\parallel$ to basal plane	ca. $170^\circ$	Avg.: 18.03; Max.: 55.32; Min.: 4.26	1.66
3		Limited nucleation along a few bands	$\parallel$ to basal plane and $\parallel$ to $\{r\}$	ca. $16^\circ$ and ca. $153^\circ$	Avg.: 13.96; Max.: 32.76; Min.: 5.09	1.59
4		Localized nucleation; minor “striped tiger” pattern and pockets of new grains	$\parallel$ to $\{m\}$ and $\parallel$ to $\{r\}$	ca. $110^\circ$ and ca. $50^\circ$	Avg.: 15.48; Max.: 41.16; Min.: 4.26	1.60



**Figure 5.** (a) Detailed BackScattered Electron (BSE) photograph showing the pitted grain boundaries of new quartz grains in Domain 1, indicative of fluid-present conditions during neo-crystallization of the new grains. Black arrows indicate grain boundary of new grain. (b) BSE image from Domain 1. Black arrows indicate grain boundaries between new grains. New grains have a slight different shade of gray, due to a channeling effect. (c) BSE image from Domain 1. Secondary calcite is present within a band. (d) BSE image from Domain 2 showing pitted grain boundaries (black arrow) and secondary calcite.





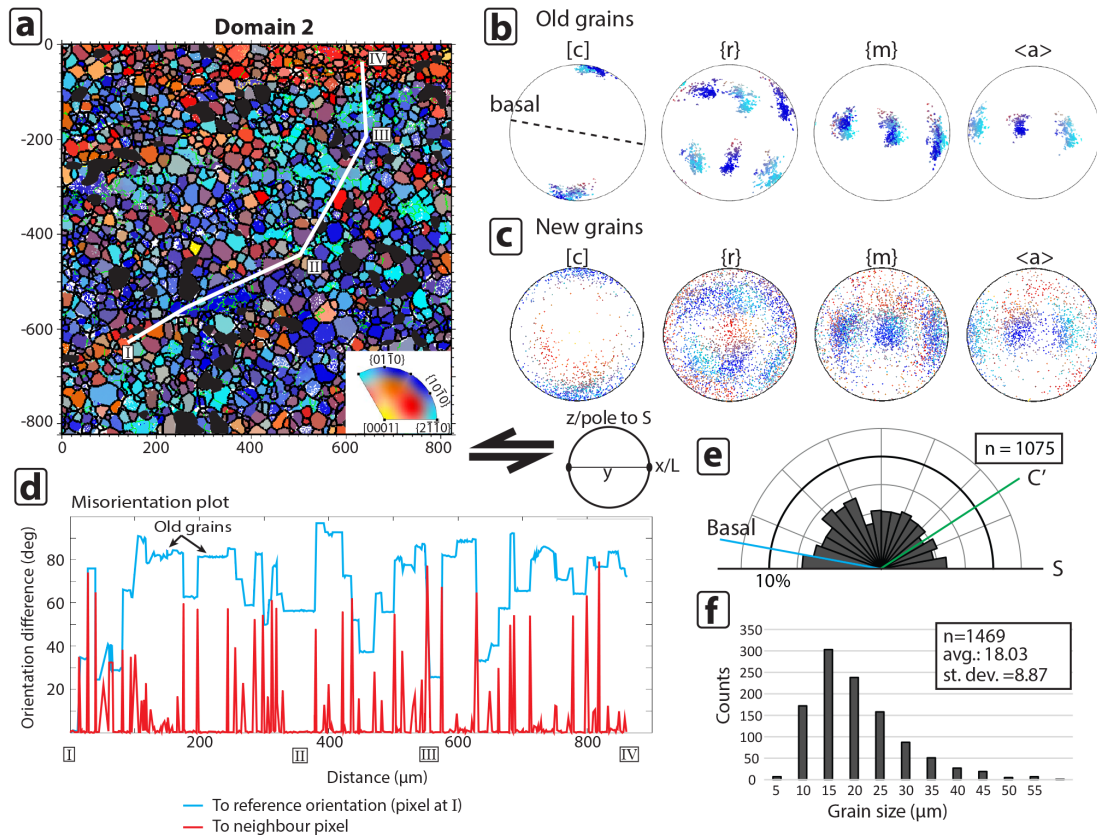
**Figure 6.** Compilation of EBSD data from Domain 1 (see Fig. 3b and c for location of the domain). **(a)** EBSD map color-coded according to the inverse pole figures (IPFs) for quartz shown in lower right corner of map. The IPF is with respect to the X direction of the finite strain ellipsoid (stretching lineation of the phyllonite). Black lines: grain boundaries defined by misorientations  $> 10^\circ$ . Green lines: subgrain boundaries defined by misorientations  $< 10^\circ$ . Black grains are calcite. White line 1 (I–IV) and 2 (I–II) are the traces of misorientation profiles in **(d)**. **(b)** and **(c)** Pole figures of quartz showing the orientation of  $\{c\}$ ,  $\{r\}$ ,  $\{m\}$  and  $\langle a \rangle$  for old and new grains, respectively. The stereograms are upper hemisphere projections of 10 000 random points. Dashed lines represent the trace of the bands of new grains and the crystallographic plane they are parallel to. **(d)** Misorientation profiles displaying difference in orientation to neighbor pixel (red line) and to reference orientation (i.e., orientation of pixel at I); blue line). **(e)** Rose diagram displaying the orientation of the long axis of the new grains with respect to the trace of  $C'$ ,  $S$  (horizontal) and the crystallographic planes that the bands are parallel to. **(f)** Histogram displaying grain size distribution of the new grains.

#### 4.2.2 Domain 2

Domain 2 is located at the tip of the quartz vein, where the latter is sandwiched by the foliation  $S$  and the micaceous shear plane  $C'$  of the host phyllonite (Fig. 3b). It contains abundant secondary calcite and cavities from sample preparation show pitted grain boundaries (Fig. 5d). Grain size distribution is unimodal. The domain is almost completely made up of new grains (Figs. 3d and 7a), although local relics of a

few host old grains (up to  $80\ \mu\text{m}$  in size) can still be recognized (Fig. 7a).

Domain 2 is pervasively recrystallized (Fig. 3d) with only small amounts of preserved old grains, as shown by the presence of local subgrain boundaries within the larger and more irregular crystals (Fig. 7a and d). The old grains form a  $c$  axis maximum around the  $Z$  direction of finite strain in the pole figure, with only a weak clockwise rotation (Fig. 7b). As far as the new grains are concerned, Domain 2 has the largest



**Figure 7.** Compilation of textural data from Domain 2 (see Fig. 3b and d for its location). **(a)** EBSD map of crystallographic orientation of quartz. Color-coding and boundary types like in Fig. 6. Black grains are calcite. White line I–IV: trace of misorientation profile in **(d)**. **(b)** and **(c)** Pole figures of quartz showing the orientation of  $[c]$ ,  $\{r\}$ ,  $\{m\}$  and  $\langle a \rangle$  for old and new grains, respectively. The stereograms are upper hemisphere projections of 10 000 random points. Dashed lines represent the trace of the bands of new grains and the crystallographic plane they are parallel to. **(d)** Misorientation profiles displaying difference in orientation to neighbor pixel (red line) and to reference orientation (i.e., orientation of pixel at I; blue line). **(e)** Rose diagram displaying the orientation of the long axis of the new grains with respect to the trace of  $C'$ ,  $S$  (horizontal) and the crystallographic planes which the bands are parallel to. **(f)** Histogram displaying grain size distribution of the new grains.

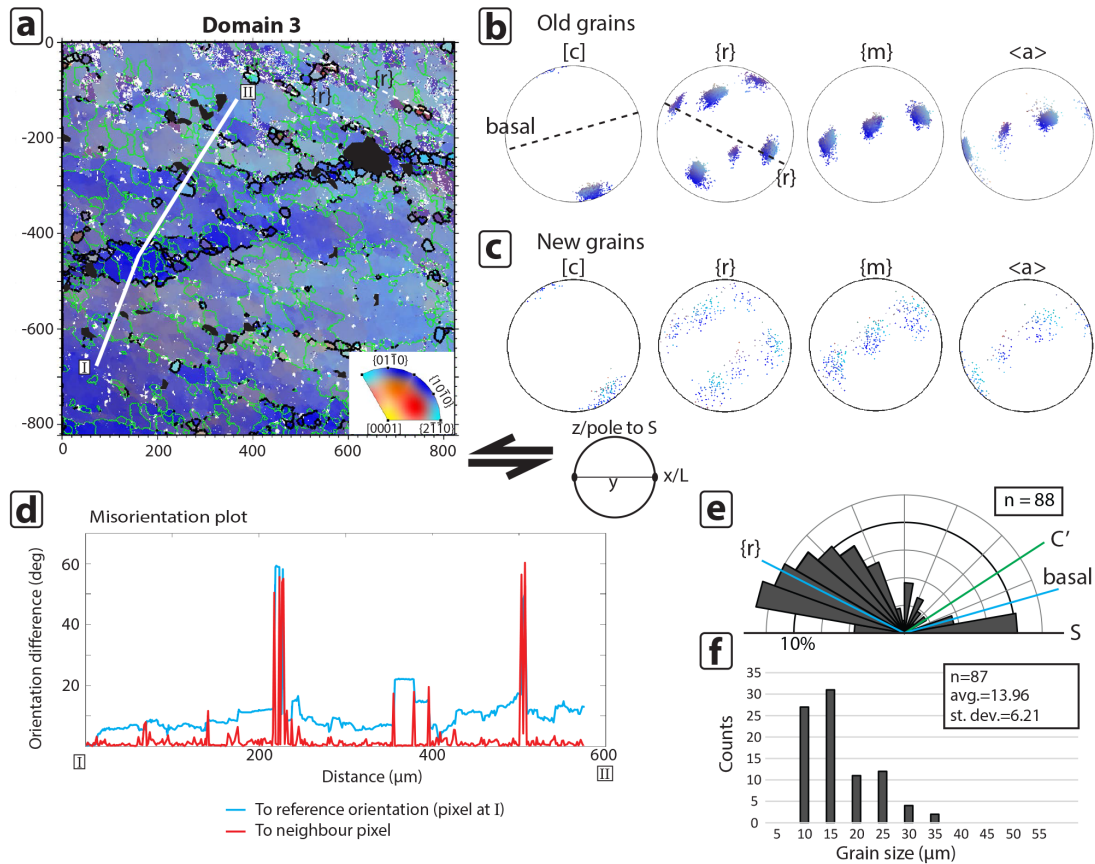
average grain size of all domains and the highest average aspect ratio, with 18.03 and 1.66  $\mu\text{m}$ , respectively (Fig. 7e, f and Table 1). There is no obvious preferred elongation direction of the new grains (Fig. 7e). The new-grain crystallographic orientations are broadly scattered around those of the old grains. The new grains have a high and sharp misorientation to each other and to the old grains, and they are relatively strain free. No progressive lattice rotation is visible towards the new grains (Fig. 7d).

#### 4.2.3 Domain 3

The upper part of the vein hosts a large grain measuring  $5 \times 3 \text{ mm}$ , which hosts Domain 3 of our study (Fig. 3b and e). The grain displays sweeping and patchy undulose extinction with upright WEBS and two sets of bands of new grains. The new grains in these bands are less developed than in other domains. The most pronounced set is recognized due to its slightly different extinction direction com-

pared to the host. Generally, there are few new grains within these bands, although some local, isolated pockets of new grains occur (Fig. 3e). The new grains are encircled by fluid inclusions and some tiny muscovite grains (ca. 20  $\mu\text{m}$ ; Fig. 4d), and their grain boundary microstructure shows evidence for porosity and solution-precipitation features (e.g., Mancktelow and Pennacchioni, 2004; Fig. 5). The bands and fluid inclusion trails define patchy undulose extinction patterns (bLEBs; Derez et al., 2014). The second set of bands is seen as semi-straight trails of small fluid inclusions (< ca. 2  $\mu\text{m}$ ), with no visible recrystallization. The left half of the domain is characterized by sub-parallel fluid inclusion trails. No nucleation of new grains is seen along these traces (white arrows in Fig. 3e).

Only local bands and clusters of new grains are observed in Domain 3, which is the domain with the lowest density of new grains (Fig. 8a). The  $c$  axis of the host old grain is sub-parallel to the  $Z$  direction of finite strain, and slightly inclined



**Figure 8.** Compilation of textural data from Domain 3 (see Fig. 3b and e for its location). **(a)** EBSD map of crystallographic orientation of quartz. Color-coding and boundary types like in Fig. 6. Black grains are calcite. White line I–II: trace of misorientation profile in **(d)**. **(b)** and **(c)** Pole figures of quartz showing the orientation of  $[c]$ ,  $\{r\}$ ,  $\{m\}$  and  $\langle a \rangle$  for old and new grains, respectively. The stereograms are upper hemisphere projections of 10 000 random points. Dashed lines represent the trace of the bands of new grains and the crystallographic plane they are parallel to. **(d)** Misorientation profiles displaying difference in orientation to neighbor pixel (red line) and to reference orientation (i.e., orientation of pixel at I; blue line). **(e)** Rose diagram displaying the orientation of the long axis of the new grains with respect to the trace of  $C'$ ,  $S$  (horizontal) and the crystallographic planes which the bands are parallel to. **(f)** Histogram displaying grain size distribution of the new grains.

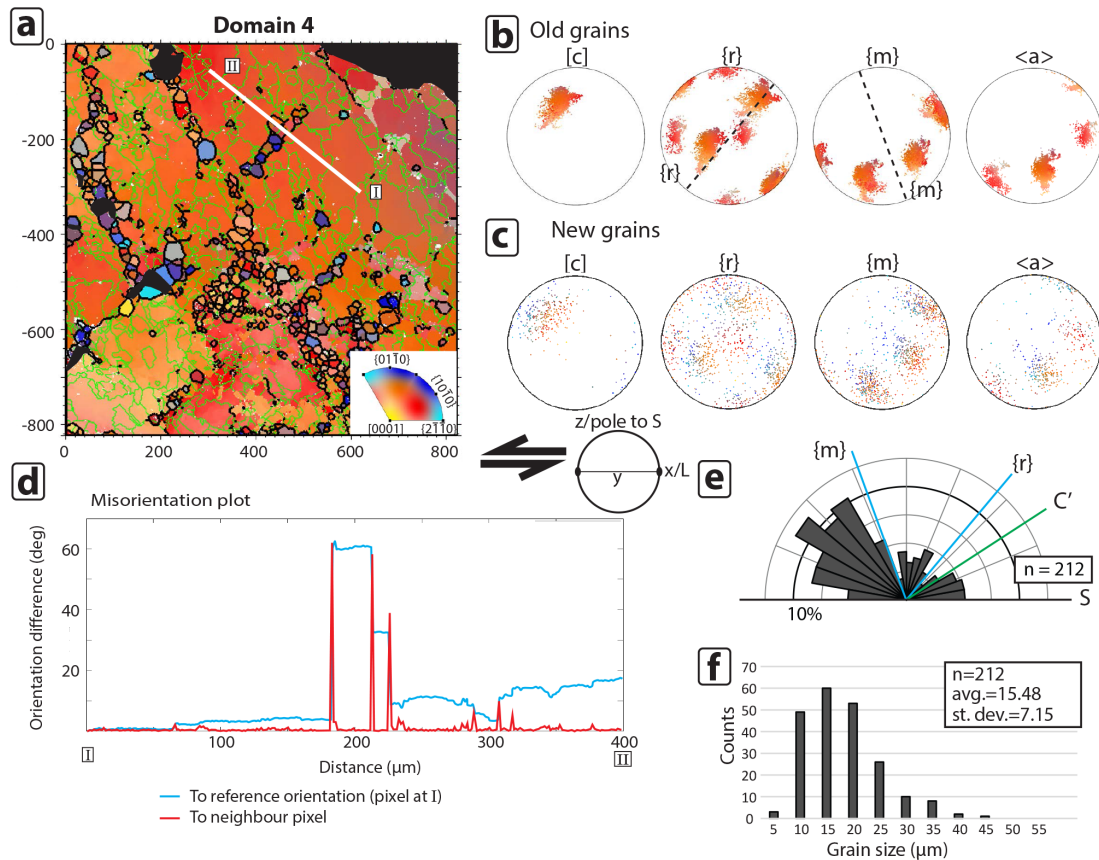
with the bulk sinistral sense of shear (Fig. 8b). The host old grains display a clear single-crystal maximum with very little dispersion of the  $c$  axis and  $\langle a \rangle$  axes, although some undulose extinction can be inferred. The bands and clusters of new grains are oriented at ca.  $16^\circ$  to the foliation  $S$ , measured counterclockwise, which makes them sub-parallel to the basal plane of the old grain (dashed line in Fig. 8b). In the central and left parts of Domain 3, fluid inclusion trails are observed. These trails are sub-parallel to the rhomb direction (white arrows in Fig. 3e, and dashed line in Fig. 8b) and are oriented at  $153^\circ$  measured counterclockwise from the foliation  $S$ .

The average grain size of the new grains is  $13.96 \mu\text{m}$  (Fig. 8e and Table 1) and they have an average aspect ratio of 1.59 (Fig. 8f) with the preferred elongation at ca.  $115^\circ$  measured counterclockwise from the foliation  $S$ . The crystallographic planes and directions of the new grains are scat-

tered around those of old grains (Fig. 8c and b, respectively). The data seem to have been rotated counterclockwise around the  $y$  axis. This domain has the smallest grain size, both average and maximum and the lowest aspect ratio (Table 1 and Fig. 8e and f). The measured misorientation profile shows that the orientation difference between neighbor old grains is quite large. Locally, subgrain boundaries grade to high-angle boundaries with misorientations in excess of the threshold value of  $10^\circ$  (black arrows in Fig. 8a and d), whereas new grains display misorientations of up to  $20^\circ$  with respect to neighbor grains (Fig. 8d). In addition, misorientation profiles locally show what appears to be a progressive lattice rotation towards the grain boundaries.

#### 4.2.4 Domain 4

Domain 4 is a relatively small, single crystal measuring  $2 \times 0.5 \text{ mm}$  (Fig. 3b and f). Above the crystal, there is a high

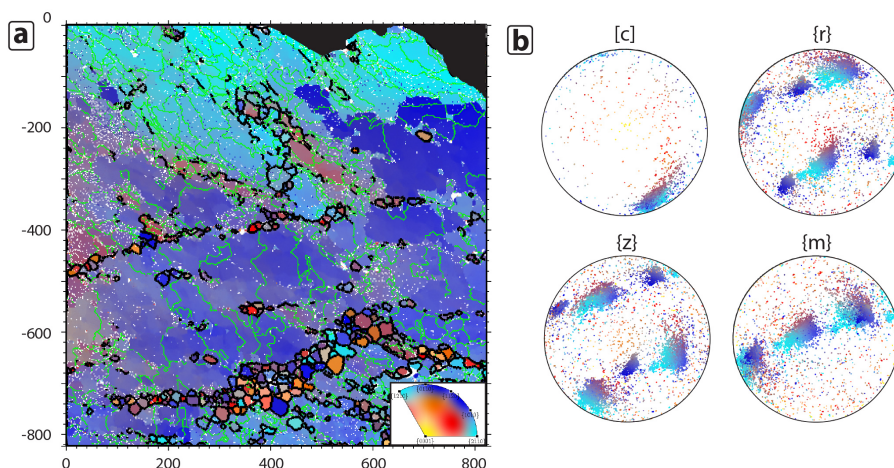


**Figure 9.** Compilation of textural data from Domain 4 (see Fig. 3b and f for its location). **(a)** EBSD map of crystallographic orientation of quartz. Color-coding and boundary types like in Fig. 6. Black grains are calcite. White line I–IV: trace of misorientation profile in **(d)**. **(b** and **c)** Pole figures of quartz showing the orientation of [c], {r}, {m} and <a> for old and new grains, respectively. The stereograms are upper hemisphere projections of 10 000 random points. Dashed lines represent the trace of the bands of new grains and the crystallographic plane they are parallel to. **(d)** Misorientation plot displaying difference in orientation to neighbor pixel (red line) and to reference orientation (i.e., orientation of pixel at I); blue line). **(e)** Rose diagram displaying the orientation of the long axis of the new grains with respect to the trace of  $C'$ ,  $S$  (horizontal) and the crystallographic planes which the bands are parallel to. **(f)** Histogram displaying grain size distribution of the new grains.

density of feldspar clasts wrapped in an anastomosed phylonitic matrix with shear indicators suggesting opposite kinematics than the top-to-the-SE regional sense of shear accommodated by the NFZ. Microstructurally the crystal resembles Domain 1, with a “striped tiger” microstructure. In Domain 4, however, two well-developed sets of bands with new grains occur, in contrast to Domain 1 where there is only one well-developed direction. One direction, inclined towards the right, is the most pronounced, whereas the one inclined to the left is slightly less pervasive. The traces of the two bands are separated by ca.  $70^\circ$ . Insertion of the lambda plate reveals that the main band of new grains also separates two subdomains within the single crystal with a slight misorientation to each other. The crystal contains some randomly arranged fluid inclusions.

Domain 4 has an old grain with a  $c$  axis located in an intermediate position between the  $z$  and  $y$  axis of strain and

slightly inclined with the bulk sinistral sense of shear (Fig. 9a and b). Undulose extinction is seen as different shades of orange in the EBSD maps, and red represents Dauphiné twins (Fig. 9a). The old grain contains some subgrains that are generally larger than the new grains. The two identified sets of bands are parallel to the prism and the rhomb and form a  $50$  and  $110^\circ$  angle, respectively, measured counterclockwise from the foliation  $S$  (dashed lines in the rhomb {r} and prism {m} pole figures in Fig. 9b and Table 1). The average aspect ratio of the new grains is 1.60 and the average grain size is  $15.48\ \mu\text{m}$  and (Fig. 9e and f) with an elongation direction of ca.  $104^\circ$  measured counterclockwise from the horizontal  $S$ . In addition, the new grains define a more scattered  $c$  axis distribution (Fig. 9c). A misorientation profile across one of the rhomb-parallel bands shows that the recrystallized grains are rather strain free, with very little internal misorientation. The boundary between the old grain and the recrystallized



**Figure 10.** (a) EBSD map crystallographic orientation of quartz of area located within Domain 3 (see Fig. 3b for location). Color-coding and boundary types like in Fig. 6. The map shows Dauphiné twins where one twin, the *r*-twin, has accommodated more viscous strain than the *z*-twin, as seen from the pole figures in (b). See text for further explanation.

bands is sharp and not progressive (Fig. 9d), although a small shift in orientation is seen across the band. Furthermore, the boundary is  $60^\circ$ , which indicates that the band might exploit a Dauphiné twin boundary.

## 5 Discussion

### 5.1 Strain accommodation history within the different domains

Our data set documents examples of quartz microstructures developed in a fluid-rich system deformed under low-grade metamorphic conditions. In our conceptual understanding, initial embrittlement of the host greenstones was accommodated by fracturing, fluid circulation and quartz (and carbonate) precipitation as vein material. The initial crystallization of the vein occurred statically, resulting in a seemingly random crystallographic orientation of the constituting large quartz crystals during the Paleoproterozoic. Later, pervasive viscous deformation led to strain accommodation within the vein and development of the ECC in the host greenstones. Viscous deformation, however, was interrupted by transient episodes of embrittlement, which we relate to both the crystallographic framework inherited from the statically crystallized vein and the oscillations of the pressure of the fluid phase that was present during continued deformation related to the thrusting history along the NFZ.

This structural evolution is summarized conceptually in Fig. 11, supported by the summary of Table 1 and discussed in detail below.

Following initial fracturing and vein crystallization (possibly related to early Caledonian deformation or even to the Paleoproterozoic evolution of the region; Fig. 11a), the vein became progressively involved in the Caledonian deforma-

tional history of the NFZ, wherein top-to-the-SE thrusting led to the progressive development of the fault zone. Environmental conditions were such that quartz began to deform by low-grade crystal-plastic deformation by dislocation glide and possibly creep (Fig. 11b). Two main mechanisms are believed to have controlled this stage of the microstructural evolution: (1) strain partitioning resulting from the high competence contrast between the vein and the surrounding greenstone, which was evolving into a progressively foliated and finer-grained phyllonite as strain was accommodated in the core of the NFZ (Trepmann and Stöckhert, 2009); and (2) presence of fluids as documented by the numerous veinlets, secondary phases trapped along grain boundaries, pitted grain boundaries and fluid inclusions (e.g., Drury and Urai, 1990; Mancktelow and Pennacchioni, 2004; Mancktelow et al., 1998; Fig. 11b). Low-grade viscous deformation produced structures such as bulging grain boundaries (Fig. 4c) caused by slow grain boundary migration (Stipp et al., 2002), sweeping undulatory extinction, subgrains, bLEBs and WEBs (Derez et al., 2014; Figs. 3b–f and 4f). EBSD analysis has shown remarkably different microstructures and CPO patterns in the analyzed domains that can be assigned to this microstructural stage. We ascribe this to the fact that each domain had a different crystallographic orientation, due to the static initial crystallization in the vein and the location of individual domains with respect to the mesoscopic structural features, such as the  $C'$  shear band.

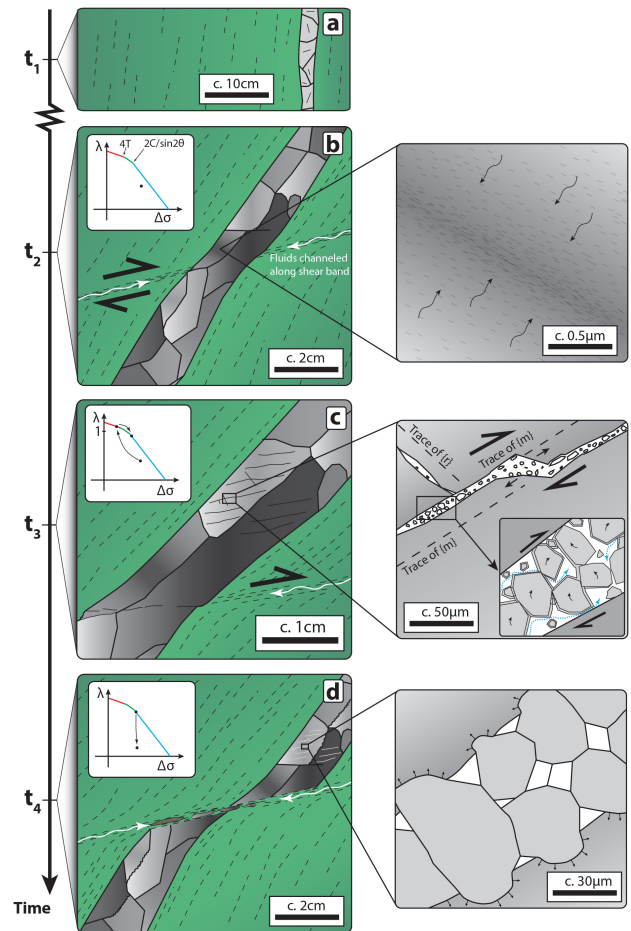
Domain 1, for example, would have been well oriented for viscous slip accommodated by either prism  $\langle a \rangle$  or  $c$  slip (Fig. 6b). In order to be activated, however, these slip planes require higher-grade conditions than those at which the vein was deforming (Schmid and Casey, 1986; Stipp et al., 2002). Synkinematic chlorite thermometry from similar faults in the area has established a peak temperature of  $< 300^\circ\text{C}$  (Torg-

ersen and Viola, 2014), ideal for activation of basal  $\langle a \rangle$  slip (e.g., Stipp et al., 2002). The crystal of Domain 1 was, however, misoriented for basal  $\langle a \rangle$  slip. Some strain was nonetheless taken up in a ductile fashion in Domain 1 by the development of WEBS (Derez et al., 2014) and possibly by dislocation creep, as shown by the subgrain boundaries. Since easy-glide planes were oriented at a high angle to the  $C'$  shear band, dislocation glide and creep soon resulted ineffective, leading to strain hardening, possibly by dislocation tangling, and localized embrittlement of the deforming quartz accommodated by fracturing. Transiently high fluid pressure is also believed to have contributed to localized and short-lived embrittlement as the fluid factor  $\lambda$  approached unit value (e.g., Cox, 2010; Hubbert and Rubey, 1959; Fig. 11c). Evidence for fluid-accompanied fracturing, such as fluid inclusion trails (Figs. 5b, c, 4d and f), is invariably found in the studied samples and within the NFZ in general.

The fractures developed during this stage of the structural evolution of Domain 1 are invariably intra-granular, which points towards sub-critical crack growth, by, for example, stress corrosion, microplasticity or general plasticity (e.g., Atkinson, 1982, 1984; Stünitz and Fitz Gerald, 1993). Development of volumetrically small gouges along the fracture planes is also envisaged (Stünitz et al., 2003; Fig. 11c, insert). The sub-parallel orientation of the fractures suggests in addition that they formed controlled by specific lattice planes, that is, planes with a low density of covalent bonds and thus low surface energy (e.g., Fairbairn, 1939; Flörke et al., 1981; Vollbrecht et al., 1999; van Daalen et al., 1999; Figs. 6, 8 and 9).

The weakest crystallographic plane in quartz is the positive rhomb, both in terms of surface energy and elastic properties (Menegon et al., 2011). Van Daalen et al. (1999) report what they refer to as “micro shear zones”, that is, bands of new grains along the positive and negative rhomb planes. The two sets of bands with nucleated new grains within Domain 1 are sub-parallel to the prism and the rhomb face of the crystal. The prism plane direction, parallel to which we find the most pervasive set of bands of new grains, was the optimally oriented direction for brittle failure, as it is sub-parallel to the actual slip plane of the mesoscopic system, that is, the  $C'$  shear band (Fig. 6e). The rhomb, although oriented at high angle to the shear band, is the weakest crystallographic plane in quartz, and, therefore, it did also fail. The geometric orientation of the rhomb was such that it was suitably oriented to accommodate strain along the antithetic direction of a conjugate set of fractures.

Furthermore, the anisotropy of the elastic properties of quartz may also have contributed to promoting preferential failure along specific crystallographic planes (Menegon et al., 2011; McSkimin et al., 1965). This is suggested by Domain 3 (small square in Fig. 3b), wherein Dauphiné twins are deformed unevenly, with the  $r$ -twin accommodating more plastic strain than the  $z$ -twin (Fig. 10a;  $r$ -twin and  $z$ -twin ter-



**Figure 11.** Conceptual sketch of the temporal evolution of the studied quartz vein with associated microstructures. See text for further details.  $\lambda - \Delta\sigma$  diagrams (Cox, 2010) illustrate the transient evolution of fluid overpressure.

minology after Menegon et al., 2011). The pole figures in Fig. 10b show that the pole to one of the positive rhombs is oriented close to the Z direction of finite strain (bulk shortening direction). This orientation corresponds to the  $r$ -twin orientation and, accordingly, the  $r$ -twin is more deformed than the  $z$ -twin (as evident from the more pronounced dispersion of the poles to  $\{r\}$  compared to the poles to  $\{z\}$ , which indicates a higher degree of internal distortion of the  $r$ -twin). The twin with the negative rhomb facing the same direction (the  $z$ -twin) is stiffer and did not accommodate the same amount of viscous strain.

In summary, the “striped tiger” microstructure observed within Domain 1 is best interpreted in terms of “sealing” of these earlier fractures by rotation of fracture fragments caused by micro-displacements and subsequent nucleation of the new grains (Fig. 11c, insert and d, insert). This mechanism is discussed in more detail in Sect. 5.2.

In contrast to Domain 1, Domain 3 was more suitably oriented for effective accommodation of viscous deformation, with the basal plane oriented close to the  $C'$  shear band, that is, well oriented for slip along the basal  $\langle a \rangle$  (Schmid and Casey, 1986). Domain 3, however, also contains two sets of bands with new grains, although more poorly developed than in Domain 1 (Figs. 3e and 8). The bands parallel to the basal planes show a larger amount of recrystallization than those parallel to the rhomb planes. Furthermore, misorientation profiles locally show a progressive misorientation from the old grain to the new grains along the basal-parallel bands. This suggests that subgrain rotation recrystallization was probably operative in Domain 3. A crystal with the orientation of Domain 3 would have been more prone to accommodate strain by dislocation glide and creep, and would thus not strain harden as much as Domain 1. In addition, one set of fractures would have had to form along the basal plane of the crystal, which is not a crystal plane with particularly low surface energy or Young's modulus. We interpret the second set, sub-parallel to the rhomb, as sealed fractures. It is worth noting that the positive rhomb is the most compliant crystallographic plane in quartz and, therefore, tends to localize fracturing (McSkimin et al., 1965; Lloyd, 2000; van Daalen et al., 1999). EBSD analysis reveals that some new grains developed also along these fractures, but mostly in the junctions where the two fracture sets intersect. However, new-grain nucleation along fracture planes parallel to the rhomb is not nearly as pervasive as along the other fracture in the same domain or any of the other fractures in Domain 1 (Figs. 8a and 6a). We suggest that these fractures opened during an earlier embrittlement event, possibly under different physical boundary conditions, wherein the fractures healed by epitaxial growth on the fracture wall, thus not creating an orientation difference, but rather parallel trails of fluid inclusions. In summary, we argue that less pervasive domainal fracturing affected Domain 3, and that crystal-plastic deformation and recovery were locally operative due to the suitable orientation of the domain for slip along the basal  $\langle a \rangle$  system.

The quartz crystal of Domain 4 was oriented similarly to the one in Domain 1 and it thus underwent only limited crystal-plastic deformation, with the latter strongly inhibited by early strain hardening, possibly promoted by dislocation tangling, resulting in undulose extinction and domainal fracturing. Similarly to Domain 1, Domain 4 is also characterized by fracturing along the prism and the rhomb planes (Fig. 9b). Both directions are fairly well developed, but the prism-parallel bands are more continuous. In this domain the rhomb-parallel set has a similar orientation as the  $C'$  shear band, while the prism-parallel set developed along the antithetic direction of the conjugate set. This fits well with the mesoscopic geometry of the vein, which is boudinaged (Fig. 3a).

Domain 2 is remarkably different from all other sites. In it, the orientation of the now almost totally obliterated old grains is similar to that of Domain 3, that is, opti-

mal for glide-accommodated creep with slip along the basal  $\langle a \rangle$ . Despite the similarity in orientation, however, the microstructures observed are remarkably different, with Domain 2 displaying a significant volume of new grains and with only very few remnants of the old grains (Figs. 3d, 7a and d). We ascribe the pervasive nucleation of Domain 2 to its location. The domain is located in a relatively high strain zone between the  $C'$  shear plane and the foliation, where the tip of the vein is dragged into the  $C'$  shear bands. We argue that Domain 2 represents a high-strain equivalent to Domain 3, where crystal-plastic deformation along the basal plane possibly coupled with nucleation and growth of new grains along rhomb-parallel fractures (like in Domain 2) resulted in extensive recrystallization. The high density of subgrain boundaries in the remnant old grain (Fig. 7a and d) suggests that crystal-plasticity has been active to the same extent as in Domain 3 and has contributed in developing the microstructures observed in the sample.

## 5.2 Sealing of the microfractures

As discussed above, domainal fractures were sealed by equigranular and slightly elongated, strain free quartz crystals that show a slight rotation about the bulk vorticity axis ( $Y$  direction of finite strain). We propose that two main mechanisms were responsible for the formation of the observed microstructure: (1) precipitation of new grains into the fracture promoted by circulating fluids (Menegon et al., 2008; Hippertt and Egydio-Silva, 1996; Vernooij et al., 2006a). New grains started to grow by a solution-precipitation mechanism promoted by the fluids that were forced into the fracture because of the high fluid pressure; and (2) as fractures propagated through the crystal, possibly by localized stress corrosion (e.g., van Daalen et al., 1999; Vernooij et al., 2006b), fragments of the host grain were ripped loose generating micro gouges, especially in volumes with jogs and geometric irregularities along the fracture planes (Fig. 11c). This mechanism explains the rotation of the crystallographic axes as shown by the EBSD data (Figs. 6c, 7c and 10c, insert). Subsequent growth of the new grains occurred either by precipitation from the actively infiltrating over pressured fluid (solution precipitation; Vernooij et al., 2006a) or by solution transfer from one pore wall to another (dissolution precipitation; Hippertt and Egydio-Silva, 1996). This model explains Domain 1 and 4, where fractures formed pervasively.

In Domain 3, where fracturing was minimal due to the favorable orientation of the crystal for basal  $\langle a \rangle$  dislocation glide, less energy was required to maintain steady state crystal-plastic deformation and significant embrittlement was not achieved; hence, no bands of new grains sealing older fractures were produced, and instead only local pockets of newly formed, strain free grains crystallized. These pockets and a few only poorly developed bands are all oriented along discrete subgrain to grain boundaries with relatively high misorientations ( $10^\circ \pm 3^\circ$ ; Fig. 8a and d), which

may have acted as conduits for fluids during deformation and initiated solution precipitation in pores and micro fractures oriented along the subgrain and grain boundaries. Fluid infiltration may also have led to hydrolytic weakening, which is known to promote local climb-accommodated dislocation creep (e.g., Kronenberg et al., 1990; Mancktelow and Pennacchioni, 2004). This could account for the few observed bands of subgrains. The growth of new grains within pores is well described by Hippertt and Egydio-Silva (1996) and results in intrapore grains, which first grow by solution precipitation followed by grain boundary migration when they touch the opposite fracture wall (Fig. 11c, insert and d, insert). Because the new grains are largely strain free, they grew at the expense of the old grains, which are more deformed and have a higher dislocation density (e.g., Drury and Urai, 1990). Furthermore, Schmid and Casey (1986) proposed that grains growing by grain boundary migration tend to grow optimally oriented for basal slip, i.e., with the basal plane at  $45^\circ$  to  $\sigma_1$  (Vernooij et al., 2006a). This mechanism could have also contributed to the rotation of the new-grain crystals seen in the EBSD data (Fig. 6).

As also proposed by several authors (e.g., Derez et al., 2014; Vernooij et al., 2006a; Trepmann et al., 2007), we conclude that dynamic recrystallization by subgrain rotation recrystallization can be excluded for the formation of the bands containing new grains in Domain 1 and 4. We base our interpretation on the following: (1) no progressive lattice rotation towards the bands of new grains is observed (Figs. 6d and 9d); (2) the new grains show large misorientations to the host (Figs. 6d and 9d) at low strains, making grain boundary sliding unlikely; (3) new grains are subhedral to euhedral with  $120^\circ$  angles between the crystal faces, indicating growth within a fluid (Hippertt and Egydio-Silva, 1996); (4) fluid inclusions encircle the new grains and their pitted grain boundaries (Figs. 4d and 5); and (5) secondary mineral phases occur between the new grains indicating that fluids penetrated the crystal (Figs. 4d, 5c and d).

New grains, however, have also accommodated some crystal-plastic deformation, because the embrittlement of the system is believed to have occurred only transiently as fluid pressure reduced the effective stresses and caused failure by brittle processes. As stress was released by the opening of intracrystalline fractures and venting of the overpressured fluid phase, viscous deformation became dominant, possibly also promoted by residual fluids (Segall and Simpson, 1986). This renewed viscous environment during ongoing deformation enhanced dislocation glide and possibly even local climb, which caused bulging grain boundaries, subgrain formation (Figs. 10d and 4c) and, as noted above, growth of new grains at the expense of old grains by grain boundary migration (Fig. 11d, insert). Vernooij et al. (2006a) and Trepmann et al. (2007) also report partially deformed new grains that show flattening and hence elongation perpendicular to  $\sigma_1$ . Recrystallization in Domain 2 and 3 was largely the result of crystal plasticity and subgrain rotation due to

the suitable orientation of the crystal for the activation of the basal  $\langle a \rangle$  slip system. Only a minor component of fracturing and neo-crystallization along the rhomb plane is envisaged.

In summary, we propose a model of alternating brittle and viscous deformation localized in intracrystalline bands hosted in vein quartz crystals (e.g., Hirth and Beeler, 2015; Fig. 4f). The relative role of subgrain rotation recrystallization as opposed to neocrystallization along microcracks is determined by the crystallographic orientation of the host grain, which results in remarkably different microstructures and internal partitioning of strain. Transmission Electron Microscope (TEM) analysis of dislocation microstructures in the interior of the old grains and next to the bands of new grains would be necessary to verify and confirm some of our conclusions.

### 5.3 Mechanical implications for the PIS development

The described microstructures and the proposed conceptual model have implications on both the local geological history and on the rheological properties of quartz and phyllonitic rocks.

The exact timing of vein emplacement remains largely unconstrained. The fact that the vein crystallized statically prior to being cut by a shear band of Caledonian age within the fault core of the NFZ and that it belongs structurally to a Caledonian imbricate structure (Torgersen and Viola, 2014; Torgersen et al., 2014) demonstrates that the vein is pre- to syntectonic. Whether the vein crystallized during the Paleoproterozoic and was later reworked during Caledonian deformation or it formed during the Paleozoic Caledonian orogeny is not known.

Irrespective of the time of initial vein formation, as the Caledonian nappes were translated towards the foreland within the highly deformed PIS, deformation localized under lower greenschist facies conditions. The host metabasalt acquired a penetrative foliation through the growth of fine-grained white mica and chlorite at the expense of feldspar, transforming the host rock into a weak phyllonite and leading to strain partitioning (Tullis and Wenk, 1994). Syndeformational carbonation reactions have been proposed as a viable mechanism for the transformation of the originally massive metabasalts into foliated, weak phyllonites (Torgersen and Viola, 2014). Progressive metabasalt phyllonitization localized strain efficiently within the NFZ due to the reduction of internal friction and grain size reduction as the rock could deform more readily by grain boundary sliding and dissolution-precipitation creep (e.g., Torgersen and Viola, 2014; St nitz and Fitz Gerald, 1993; Bos and Spiers, 2002). Within such a structural framework, plagioclase and quartz represented relatively competent porphyroclasts, deforming predominantly by fracturing (Fig. 4a). The studied quartz vein remained mostly unaffected by phyllonitization, thus becoming a rigid object that escaped most deformation (Bell, 1985; Menegon et al., 2008; Tullis and Wenk, 1994), although some disso-



lution at the vein-matrix contact may have occurred (white arrows in Fig. 3b). The progressively increasing competence contrast between the phyllonitic matrix and the quartz vein generated significant strain partitioning, wherein coaxial deformation was accommodated by the quartz vein (e.g., the described conjugate shear bands) and non-coaxial deformation by the matrix, as shown by, for example, rotated porphyroclasts and asymmetric shear bands (e.g., Goodwin and Tikoff, 2002; Menegon et al., 2008). This rheological contrast is also believed to be crucial for the transient embrittlement of the quartz vein as already argued for in the discussion above. Both the phyllonite *S* and *C'* planes, due to their interconnected anastomosing geometry and low coefficient of friction, deformed at a significantly higher strain rate than the quartz vein. This contrast enhanced quartz strain hardening, possibly by dislocation tangling within the vein, because deformation mechanisms within the matrix (such as dissolution-precipitation creep and grain boundary sliding) were much more effective than glide-accommodated dislocation creep.

The NFZ deformed in a fluid-rich system as shown by a plethora of microstructures within both the matrix and the vein quartz (e.g., Fig. 4). Several authors have stressed the importance of fluids in promoting viscous deformation in quartz (e.g., Kronenberg and Tullis, 1984; Mancktelow and Pennacchioni, 2004) and the role played by fracturing in distributing fluids within a rigid body located in a weak matrix (Menegon et al., 2008). Calcite veinlets within the *C'* shear bands indicate multiple opening events and thus point towards a fluid pressure cyclicity ( $\lambda/\Delta\sigma$  plot in Fig. 11b–d). Similar conditions are also described from other parts of the PIS, such as the Kvenklubben Fault some kilometers west of the NFZ (Torgersen and Viola, 2014).

Although the weak phyllonitic core of the NFZ could be interpreted as suggesting that the fault deformed mainly by aseismic creep, the current fault architecture has to be projected against its temporal dynamic evolution. Initial strain accommodation occurred in fact under different rheological conditions, with transient embrittlement of a >20 m thick dolostone layer possibly inducing seismic stick-slip behavior as also suggested by other localities within the PIS. Comparison of the microstructures described here with the results of Trepmann et al. (2007) and the work by Hirth and Beeler (2015) corroborates the interpretation of the NFZ as a fault that possibly accommodated coseismic deformation.

The cyclic fluid overpressuring in the NFZ might have played an important role in steering deformation towards a more discrete accommodation style, resulting in cyclic oscillations between brittle and viscous deformation in a fault-valve behavior that facilitated the translation of the Caledonian nappes to the foreland (Viola et al., 2006), but also possibly promoted seismic activity by stick-slip behavior.

## 6 Conclusions

The microstructures presented in this study contribute to the refined understanding of the mechanisms that accommodate strain in quartz during deformation at the brittle–viscous transition. Our observations confirm results from earlier studies and in addition allow refining existing conceptual models by showing the following.

1. Under fluid-rich conditions typical of lower greenschist facies metamorphism, quartz may fracture pervasively along several intracrystalline planes such as the prism, the rhomb, and, to a minor extent, the basal plane. The exploited direction of preferential fracturing depends on the orientation of the crystallographic planes with respect to the imposed stress field.
2. Viscous weakening mechanisms, such as effective crystal-plastic deformation, may reduce the need for embrittlement. However, if crystals are misoriented for optimal dislocation glide, strain hardening occurs, which promotes the onset of fracturing. Microfracturing and viscous deformation may occur, however, broadly coevally and cyclically.
3. Nucleation processes can heal and seal the microfractures. Solution-precipitation is the mechanism believed to control the process. Only minor recovery by sub-grain rotation recrystallization is observed, selectively on those grains suitably oriented for slip on the basal  $\langle a \rangle$  system.
4. Cyclic fluid pressure oscillations promoted continuous switches in deformation mechanisms that resulted in transient and possibly seismogenic brittle deformation processes. Aseismic creep rapidly followed these as fluids were vented, and the host phyllonite developed a penetrative, thoroughgoing anastomosing network of weak slip planes.
5. Fluid-assisted breakdown of the host metabasalt formed the weak phyllonite, which promoted strain partitioning into the matrix rather than in the quartz vein, which escaped most strain. Rheological contrasts between the weak, foliated host and the more rigid quartz vein also contributed to the transient embrittlement of quartz in the vein, providing positive feedback to the embrittlement caused by the presence of overpressured fluids.

*Acknowledgements.* The Geological Survey of Norway and the Norwegian University of Science and Technology have supported financially the preparation of this manuscript. The reviewers, Luis Morales and Michel Bestmann, are thanked for their constructive comments and input. The guest editor Giorgio Pennacchioni is thanked for important suggestions and a very efficient editorial

handling. Tine Derez is thanked for constructive feedback. Espen Torgersen is warmly thanked for very many long and fruitful discussions!

Special Issue: “Deformation mechanisms and ductile strain localization in the lithosphere”

Edited by: L. Menegon, G. Pennacchioni, M. Stipp, N. Mancktelow, and R. Law

## References

- Adams, B. L., Wright, S. I., and Kunze, K.: Orientation imaging: the emergence of a new microscopy, *Metall. Trans. A*, 24, 819–831, 1993.
- Atkinson, B. K.: Subcritical crack propagation in rocks: theory, experimental results and applications, *J. Struct. Geol.*, 4, 41–56, 1982.
- Atkinson, B. K.: Subcritical crack growth in geological materials, *J. Geophys. Res.-Sol. Ea.*, 89, 4077–4114, 1984.
- Bachmann, F., Hielscher, R., and Schaeben, H.: Texture analysis with MTEX-free and open source software toolbox, *Sol. St. Phen.*, 160, 63–68, 2010.
- Bell, T.: Deformation partitioning and porphyroblast rotation in meta-morphic rocks: a radical reinterpretation, *J. Metamorph. Geol.*, 3, 109–118, 1985.
- Bestmann, M. and Prior, D. J.: Intragranular dynamic recrystallization in naturally deformed calcite marble: diffusion accommodated grain boundary sliding as a result of subgrain rotation recrystallization, *J. Struct. Geol.*, 25, 1597–1613, 2003.
- Bos, B. and Spiers, C. J.: Frictional-viscous flow of phyllosilicate-bearing fault rock: Microphysical model and implications for crustal strength profiles, *J. Geophys. Res.-Sol. Ea.*, 107, ECV 1-1–ECV 1-13, doi:10.1029/2001JB000301, 2002.
- Chen, Y., Hjelen, J., Gireesh, S., and Roven, H.: Optimization of EBSD parameters for ultra-fast characterization, *J. Microsc.-Oxford*, 245, 111–118, 2012.
- Cox, S. F.: The application of failure mode diagrams for exploring the roles of fluid pressure and stress states in controlling styles of fracture-controlled permeability enhancement in faults and shear zones, *Geofluids*, 10, 217–233, 2010.
- Dallmeyer, R. D., Mitchell, J. G., Pharaoh, T. C., Reuter, A., and Andresen, A.: K–Ar and Ar-40/Ar-39 whole-rock ages of slate phyllite from allochthonous basement and cover in the tectonic windows of Finnmark, Norway – evaluating the extent and timing of caledonian tectonothermal activity, *Geol. Soc. Am. Bull.*, 100, 1493–1501, doi:10.1130/0016-7606(1988)100<1493:Kaaaw>2.3.Co;2, 1988.
- Dell’Angelo, L. N. and Tullis, J.: Textural and mechanical evolution with progressive strain in experimentally deformed aplite, *Tectonophysics*, 256, 57–82, 1996.
- den Brok, S. W. J.: An Experimental Investigation into the Effect of Water on the Flow of Quartzite, Utrecht University, Holland, 1992.
- den Brok, S. W. J. and Spiers, C.: Experimental evidence for water weakening of quartzite by microcracking plus solution-precipitation creep, *J. Geol. Soc. London*, 148, 541–548, 1991.
- Derez, T., Pennock, G., Drury, M., and Sintubin, M.: Low-temperature intracrystalline deformation microstructures in quartz, *J. Struct. Geol.*, doi:10.1016/j.jsg.2014.07.015, online first, 2014.
- Drury, M. R. and Urai, J. L.: Deformation-related recrystallization processes, *Tectonophysics*, 172, 235–253, 1990.
- Fairbairn, H.: Correlation of quartz deformation with its crystal structure, *Am. Mineral.*, 24, 351–368, 1939.
- Flörke, O. W., Mielke, H. G., Weichert, J., and Kulke, H.: Quartz with rhombohedral cleavage from Madagascar, *Am. Mineral.*, 66, 596–600, 1981.
- Frondel, C., Dana, J. D., and Dana, E. S.: *The System of Mineralogy: Silica Minerals*, Wiley, New York, 1962.
- Gee, D. G., Fossen, H., Henriksen, N., and Higgins, A. K.: From the early Paleozoic platforms of Baltica and Laurentia to the Caledonide Orogen of Scandinavia and Greenland, *Episodes*, 31, 44–51, 2008.
- Goodwin, L. B. and Tikoff, B.: Competency contrast, kinematics, and the development of foliations and lineations in the crust, *J. Struct. Geol.*, 24, 1065–1085, 2002.
- Hippert, J. and Egydio-Silva, M.: New polygonal grains formed by dissolution–re-deposition in quartz mylonite, *J. Struct. Geol.*, 18, 1345–1352, 1996.
- Hirth, G. and Beeler, N.: The role of fluid pressure on frictional behavior at the base of the seismogenic zone, *Geology*, 43, 223–226, 2015.
- Hirth, G. and Tullis, J.: Dislocation creep regimes in quartz aggregates, *J. Struct. Geol.*, 14, 145–159, doi:10.1016/0191-8141(92)90053-Y, 1992.
- Holyoke, C. W. and Tullis, J.: Mechanisms of weak phase interconnection and the effects of phase strength contrast on fabric development, *J. Struct. Geol.*, 28, 621–640, 2006.
- Hubbert, M. K. and Rubey, W. W.: Role of fluid pressure in mechanics of overthrust faulting, I. Mechanics of fluid-filled porous solids and its application to overthrust faulting, *Geol. Soc. Am. Bull.*, 70, 115–166, 1959.
- Kronenberg, A. K. and Tullis, J.: Flow strengths of quartz aggregates: grain size and pressure effects due to hydrolytic weakening, *J. Geophys. Res.-Sol. Ea.*, 89, 4281–4297, 1984.
- Kronenberg, A. K., Segall, P., and Wolf, G. H.: Hydrolytic weakening and penetrative deformation within a natural shear zone, in: *The Brittle–Ductile Transition in Rocks*, American Geophysical Union, Washington, D.C., 21–36, 1990.
- Lloyd, G. E.: Grain boundary contact effects during faulting of quartzite: an SEM/EBSD analysis, *J. Struct. Geol.*, 22, 1675–1693, 2000.
- Mainprice, D., Hielscher, R., and Schaeben, H.: Calculating anisotropic physical properties from texture data using the MTEX open-source package, *Geol. Soc. Spec. Publ.*, 360, 175–192, 2011.
- Mancktelow, N. S. and Pennacchioni, G.: The influence of grain boundary fluids on the microstructure of quartz-feldspar mylonites, *J. Struct. Geol.*, 26, 47–69, 2004.
- Mancktelow, N. S., Grujic, D., and Johnson, E. L.: An SEM study of porosity and grain boundary microstructure in quartz mylonites, Simplon Fault Zone, Central Alps, *Contrib. Mineral. Petrol.*, 131, 71–85, 1998.

- McSkimin, H., Andreatch Jr, P., and Thurston, R.: Elastic moduli of quartz versus hydrostatic pressure at 25 and  $-195.8^{\circ}\text{C}$ , *J. Appl. Phys.*, 36, 1624–1632, 1965.
- Menegon, L., Pennacchioni, G., Heilbronner, R., and Pittarello, L.: Evolution of quartz microstructure and *c*-axis crystallographic preferred orientation within ductilely deformed granitoids (Arolla unit, Western Alps), *J. Struct. Geol.*, 30, 1332–1347, doi:10.1016/j.jsg.2008.07.007, 2008.
- Menegon, L., Piazzolo, S., and Pennacchioni, G.: The effect of Dauphiné twinning on plastic strain in quartz, *Contrib. Mineral. Petrol.*, 161, 635–652, doi:10.1007/s00410-010-0554-7, 2011.
- Moen, K., Hjelen, J., and Malvik, T.: Preparation of Quartz samples for EBSD analysis, poster presented at the Applied Mineralogy '03 Conference, Helsinki, 17–18 March 2003.
- Pharaoh, T.: Volcanic and geochemical stratigraphy of the Nussir Group of Arctic Norway – an early Proterozoic greenstone suite, *J. Geol. Soc.*, 142, 259–278, 1985.
- Pharaoh, T., Macintyre, R., and Ramsay, D.: K–Ar age determinations on the Raipas suite in the Komagfjord Window, Northern Norway, *Norsk Geol. Tidsskr.*, 62, 51–57, 1982.
- Pharaoh, T. C., Ramsay, D. M., and Jansen, Ø.: Stratigraphy and structure of the northern part of the Repparfjord-Komagfjord Window, Finnmark, Northern Norway, *Norg. Geol. Unders. B.*, 337, 1–45, 1983.
- Platt, J. and Vissers, R.: Extensional structures in anisotropic rocks, *J. Struct. Geol.*, 2, 397–410, 1980.
- Prior, D. J., Boyle, A. P., Brenker, F., Cheadle, M. C., Day, A., Lopez, G., Peruzzo, L., Potts, G. J., Reddy, S., and Spiess, R.: The application of electron backscatter diffraction and orientation contrast imaging in the SEM to textural problems in rocks, *Am. Mineral.*, 84, 1741–1759, 1999.
- Prior, D. J., Mariani, E., and Wheeler, J.: EBSD in the earth sciences: applications, common practice, and challenges, in: *Electron Backscatter Diffraction in Materials Science*, Springer US, 345–360, doi:10.1007/978-0-387-88136-2\_26, 2009.
- Rice, A. H. N.: Stretching lineations and structural evolution of the Kalak Nappe Complex (Middle Allochthon) in the Repparfjord–Faegfjord area, Finnmark, northern Norway, *Norsk Geol. Tidsskr.*, 78, 277–289, 1998.
- Roberts, D.: The Scandinavian Caledonides: event chronology, paleogeographic settings and likely modern analogues, *Tectonophysics*, 365, 283–299, doi:10.1016/S0040-1951(03)00026-X, 2003.
- Schmid, S. and Casey, M.: Complete fabric analysis of some commonly observed quartz *c*-axis patterns, in: *Mineral and Rock Deformation: Laboratory Studies: The Paterson Volume*, American Geophysical Union, Washington, D.C., 263–286, doi:10.1029/GM036p0263, 1986.
- Schneider, C. A., Rasband, W. S., Eliceiri, K. W., Schindelin, J., Arganda-Carreras, I., Frise, E., Kaynig, V., Longair, M., Pietzsch, T., and Preibisch, S.: 671 nih image to imageJ: 25 years of image analysis, *Nat. Methods*, 9, 671–675, doi:10.1038/nmeth.2089, 2012.
- Segall, P. and Simpson, C.: Nucleation of ductile shear zones on dilatant fractures, *Geology*, 14, 56–59, 1986.
- Stipp, M. and Kunze, K.: Dynamic recrystallization near the brittle–plastic transition in naturally and experimentally deformed quartz aggregates, *Tectonophysics*, 448, 77–97, 2008.
- Stipp, M., Stunitz, H., Heilbronner, R., and Schmid, S. M.: The eastern Tonale fault zone: a “natural laboratory” for crystal plastic deformation of quartz over a temperature range from 250 to 700 degrees C, *J. Struct. Geol.*, 24, 1861–1884, doi:10.1016/S0191-8141(02)00035-4, 2002.
- Stunitz, H. and Fitz Gerald, J.: Deformation of granitoids at low metamorphic grade. II: Granular flow in albite-rich mylonites, *Tectonophysics*, 221, 299–324, 1993.
- Stunitz, H., Fitz Gerald, J., and Tullis, J.: Dislocation generation, slip systems, and dynamic recrystallization in experimentally deformed plagioclase single crystals, *Tectonophysics*, 372, 215–233, 2003.
- Torgersen, E. and Viola, G.: Structural and temporal evolution of a reactivated brittle–ductile fault – Part I: Fault architecture, strain localization mechanisms and deformation history, *Earth Planet. Sc. Lett.*, 407, 205–220, doi:10.1016/j.epsl.2014.09.019, 2014.
- Torgersen, E., Viola, G., Zwingmann, H., and Harris, C.: Structural and temporal evolution of a reactivated brittle–ductile fault – Part II: Timing of fault initiation and reactivation by K–Ar dating of synkinematic illite/muscovite, *Earth Planet. Sc. Lett.*, 407, 221–233, 2014.
- Trepmann, C. A. and Stöckhert, B.: Microfabric of folded quartz veins in metagreywackes: dislocation creep and subgrain rotation at high stress, *J. Metamorph. Geol.*, 27, 555–570, doi:10.1111/j.1525-1314.2009.00842.x, 2009.
- Trepmann, C. A., Stöckhert, B., Dörner, D., Moghadam, R. H., Küster, M., and Röller, K.: Simulating coseismic deformation of quartz in the middle crust and fabric evolution during postseismic stress relaxation – an experimental study, *Tectonophysics*, 442, 83–104, 2007.
- Tullis, J. and Wenk, H.-R.: Effect of muscovite on the strength and lattice preferred orientations of experimentally deformed quartz aggregates, *Mat. Sc.d Eng. A-Struct.*, 175, 209–220, 1994.
- van Daalen, M., Heilbronner, R., and Kunze, K.: Orientation analysis of localized shear deformation in quartz fibres at the brittle–ductile transition, *Tectonophysics*, 303, 83–107, doi:10.1016/S0040-1951(98)00264-9, 1999.
- Vernooij, M. G., den Brok, B., and Kunze, K.: Development of crystallographic preferred orientations by nucleation and growth of new grains in experimentally deformed quartz single crystals, *Tectonophysics*, 427, 35–53, 2006a.
- Vernooij, M. G., Kunze, K., and den Brok, B.: “Brittle”shear zones in experimentally deformed quartz single crystals, *J. Struct. Geol.*, 28, 1292–1306, 2006b.
- Viola, G., Mancktelow, N. S., and Miller, J. A.: Cyclic frictional–viscous slip oscillations along the base of an advancing nappe complex: insights into brittle–ductile nappe emplacement mechanisms from the Naukluft Nappe Complex, central Namibia, *Tectonics*, 25, TC3016, doi:10.1029/2005tc001939, 2006.
- Vollbrecht, A., Stipp, M., and Olesen, N. Ø.: Crystallographic orientation of microcracks in quartz and inferred deformation processes: a study on gneisses from the German Continental Deep Drilling Project (KTB), *Tectonophysics*, 303, 279–297, 1999.